Advanced Optical Materials

ADVANCED OPTICAL MATERIALS
www.advopticalmat.de

RESEARCH ARTICLE OPEN ACCESS

Electrically Reconfigurable Nonvolatile Transmissive Metasurface in Visible

Virat Tara[1] | Romil Audhkhasi[1] | Andrew Tang[1] | Rui Chen[1,2] | Johannes E. Fröch[1] | Abhinav Kala[1] | Juejun Hu[2] | Arka Majumdar[1,3]

[1]Department of Electrical and Computer Engineering, University of Washington, Seattle, Washington, USA | [2]Department of Materials Science and Engineering, Massachusetts Institute of Technology, Cambridge, Massachusetts, USA | [3]Department of Physics, University of Washington, Seattle, Washington, USA

Correspondence: Virat Tara (vtara@uw.edu) | Arka Majumdar (arka@uw.edu)

Received: 28 November 2025 | **Revised:** 18 January 2026 | **Accepted:** 5 February 2026

Keywords: antimony trisulfide | guided mode resonance | metasurfaces | phase change materials

ABSTRACT

The synergy between metasurfaces and non-volatile phase change materials (PCMs) has created many reconfigurable photonic devices for applications in optical memory, optical computing, and optical communications. But these advances have been limited to the infrared wavelengths due to the high loss of PCMs in the visible regime. Here, we demonstrate a nonvolatile visible metasurface that is electrically reconfigurable using wide bandgap PCM Sb_2S_3. Our device supports a resonant mode at 610 nm, a wavelength largely under-explored for PCM-based metasurfaces. By incorporating only a 20 nm thick layer of Sb_2S_3, we experimentally demonstrate a resonance tuning range of 16 nm. Reversible switching of the metasurface is accomplished in situ using a carefully engineered, ultrathin doped silicon micro-heater. Our work paves the way for integrating PCMs into visible-frequency systems, particularly for human-centric applications such as augmented and virtual reality displays.

1 | Introduction

Metasurfaces utilizing subwavelength scatterers can precisely manipulate the wavefront of light, enabling them to perform complex optical functions in areas such as imaging [1, 2], sensing [3], and computation [4]. However, a significant limitation of these metasurfaces is their fixed optical functionality once fabricated. Researchers explored various methods, including thermo-optic effect [5], electro-optic effect [6], liquid crystals (LCs) [7], and phase change materials (PCMs) [8–10], to modify the metasurface's response post-fabrication. All these methods essentially rely on tuning the electromagnetic (EM) modes supported by the metasurface by changing the refractive index of one of its constituent materials.

Among these above-mentioned tuning mechanisms, PCMs are particularly promising due to their non-volatile operation, which obviates the need for a constant power supply to hold the changed state. Moreover, they can provide a significant change in refractive index ($\Delta n \sim 1$) as they switch between their amorphous (a) and crystalline (c) states, as compared to other methods (for example, Δn for LC is ~ 0.2) [11]. This implies that they can perform the same operation in a smaller form factor without any thermal or electric-field crosstalk in steady state. Furthermore, PCMs' device-level integration can be further enhanced to provide deterministic multi-level operation by using meticulously designed heaters [12] beyond binary operations. Despite their many advantages, PCMs have been primarily limited to the near-infrared [8] and longer wavelengths [10] due to their high optical absorption in the visible spectrum [13]. Incorporating PCMs in the visible spectrum would unlock several new possibilities for applications like low-power dynamic displays [14], inkless e-papers [15], and local dimming of pixels in AR displays using unpolarized light [13]. Conventional polarized dimming is used

by employing liquid crystals, which leads to a significant loss of light even in the transmitting state, due to the presence of polarizers.

Fortunately, recently rediscovered PCM Antimony Trisulfide (Sb_2S_3) [15–17] is known to have a wide to have a wide tunable bandgap between 2.0 and 1.7 eV. Making it a low-loss material for wavelengths greater than 600 nm when the material is in its amorphous phase. This, along with its significant index contrast ($\Delta n = 0.68$ at 600 nm), makes Sb_2S_3 highly attractive for tunable meta-optic applications in the visible. The index contrast is induced by the micro-structural phase transition of the material from a- to c- state upon heating. Past works with Sb_2S_3 in the visible have either struggled to demonstrate reversible switching [18] when the material is integrated with a metasurface [19, 20] or have relied on heating by a laser for inducing a one-way (c- to a-) phase transition in the material [15, 16]. The a- to c- transition whereas, is carried out using furnace annealing, which takes 1 h [16]. Furthermore, laser switching requires bulky, precisely aligned setups that are impractical for large-scale commercial applications. Electrical control, on the other hand, provides an in situ solution to the above problems. Moreover, past works using laser switching [15, 16] have not been able to achieve High-Quality-factor resonances and a- to c- and c- to a- switching using a laser. This underlines the difficulty of integrating Sb_2S_3 with metasurfaces and achieving reversible switching.

In this work, we design and experimentally demonstrate a reversibly tunable transmissive metasurface in the visible frequency regime using wide-bandgap PCM Sb_2S_3. To do so, we overcome several challenges, for example lack of suitable transparent conductive materials that can be used as micro-heaters in the visible and growth dominated crystallization of Sb_2S_3 [21]. In situ electrical switching of the metasurface's optical response is achieved via a doped microheater fabricated using a Silicon (Si) on Sapphire (SOS) substrate. To minimize the losses of Si while avoiding very high resistance, we thin it down to just 55 nm. By engineering the EM mode supported by the metasurface to have a strong field overlap with the PCM layer, we achieve a 19 nm spectral shift in the transmission dip with only 20 nm of unpatterned Sb_2S_3. Furthermore, the unpatterned, blanket Sb_2S_3 film helps in promoting crystallization. Using Rapid Thermal Annealing (RTA), we are able to observe a 14 nm spectral shift in the experiment, accompanied by a 38% change in transmission amplitude at a wavelength of 671 nm. Finally, we perform in situ switching of the metasurface using electrical pulses and observe a reversible change in its resonance wavelength as large as 16 nm. We believe our work paves the way for compact, non-volatile reconfigurable meta-optics in the visible for applications ranging from quantum photonics [22, 23] to holographic displays [24, 25].

2 | Results

Our proposed transmissive metasurface consists of an ultra-thin 55 nm thick layer of crystalline-Si on a Sapphire substrate, followed by a 20 nm thick Sb_2S_3 layer, a 40 nm Al_2O_3 passivation layer [26], and a 100 nm metasurface made of non-stoichiometric silicon nitride SiN_x. Figure 1A,B shows the perspective and side views of the metasurface. We note that although Si is lossy in the visible wavelength range, it offers a significant advantage [1] of CMOS compatibility and ease of device-level integration over its alternatives in the visible spectrum, like Indium-Tin Oxide (ITO) [27], Graphene [28], and Silicon Carbide (SiC). A comparison of losses from Si of different thicknesses is shown in Figure S1, indicating a relatively low absorption of 1.5% at 600 nm induced by the 55 nm thick crystalline silicon. The use of unpatterned Sb_2S_3 in the metasurface allows us to achieve a larger resonance shift compared to conformal Sb_2S_3 (see Figure S2). Moreover, it promotes crystallization in the material. The refractive index of Sb_2S_3 measured using ellipsometry is shown in Figure 1C (for measurement details, see Supporting Text).

The unit cell, with periodic boundary conditions applied to the in-plane directions and a Perfectly Matched Layer (PML) in the out-of-plane direction, was simulated using Lumerical FDTD software. The device was illuminated using a plane wave source. The incident electric field polarization is maintained along the *x*-axis as shown in Figure 1A. The refractive indices of Si and Sapphire were used from the built-in Lumerical material library. Refractive index for the capping layer (alumina) and SiN_x (for films deposited in-house) was measured using an ellipsometer. The values for the real part of refractive index (n) were roughly 1.63 and 2.0 for Alumina and SiN_x. Figure 1D presents the spectrum of the meta-optics with a periodicity (P) of 340 nm and the grating width (W) of 100 nm. The simulated resonance wavelength redshifts by 19 nm as we switch the refractive index of Sb_2S_3 from a- to c- state. This resonance shift is accompanied by a decrease in the quality factor (Q-factor) from 230 to 102, due to the higher loss of Sb_2S_3 in the c- state. The resonant mode when in a- state also supports a 2π phase shift in reflection [29], as shown in Figure S3. Therefore, this structure can also be used for phase modulation applications in reflection [30]. Figure 1E presents the change in resonant wavelength as the periodicity of the meta-atom is swept from 300 to 380 nm. This linear scaling of the resonance wavelength to periodicity helps in setting the desirable resonant wavelength during fabrication.

Further simulations were performed to analyze and optimize the metasurface response. Figure 2A shows the field profile of the Transverse Magnetic (TM) mode inside the cavity at the resonant wavelength when Sb_2S_3 is in a- state. The incident electric field is polarized along the x-direction. Due to the ultra-low thickness of the Si slab, the mode is loosely confined in the Si slab, and therefore it largely resides outside the high-index, lossy Si slab. Furthermore, due to the EM boundary conditions, we see a step increase in the field inside the Sb_2S_3 layer, given by the following relation $E_{SbS} = (\frac{n_{Si}}{n_{SbS}})^2 \times E_{Si}$. In contrast, increasing the Si thickness increases the mode overlap with the lossy Si slab [31]. Figure 2B presents the field intensity summed along the *x*-axis of the device, showing minimal electric field inside the Si layer.

Figure 2C presents the simulated transmission spectrum for four different Si layer thicknesses. To ensure that the transmission dip shows up at approximately a wavelength of 670 nm, we tuned the grating period from 380 to 200 nm for Si layer thicknesses varying from 30 to 150 nm while keeping the other parameters fixed. We observe that as the Si layer thickness increases, the transmission dip becomes broader. This can be attributed to an increase in the resonant mode overlap with the Si layer for larger thicknesses (see Figure S4 for the electric field intensity profile in

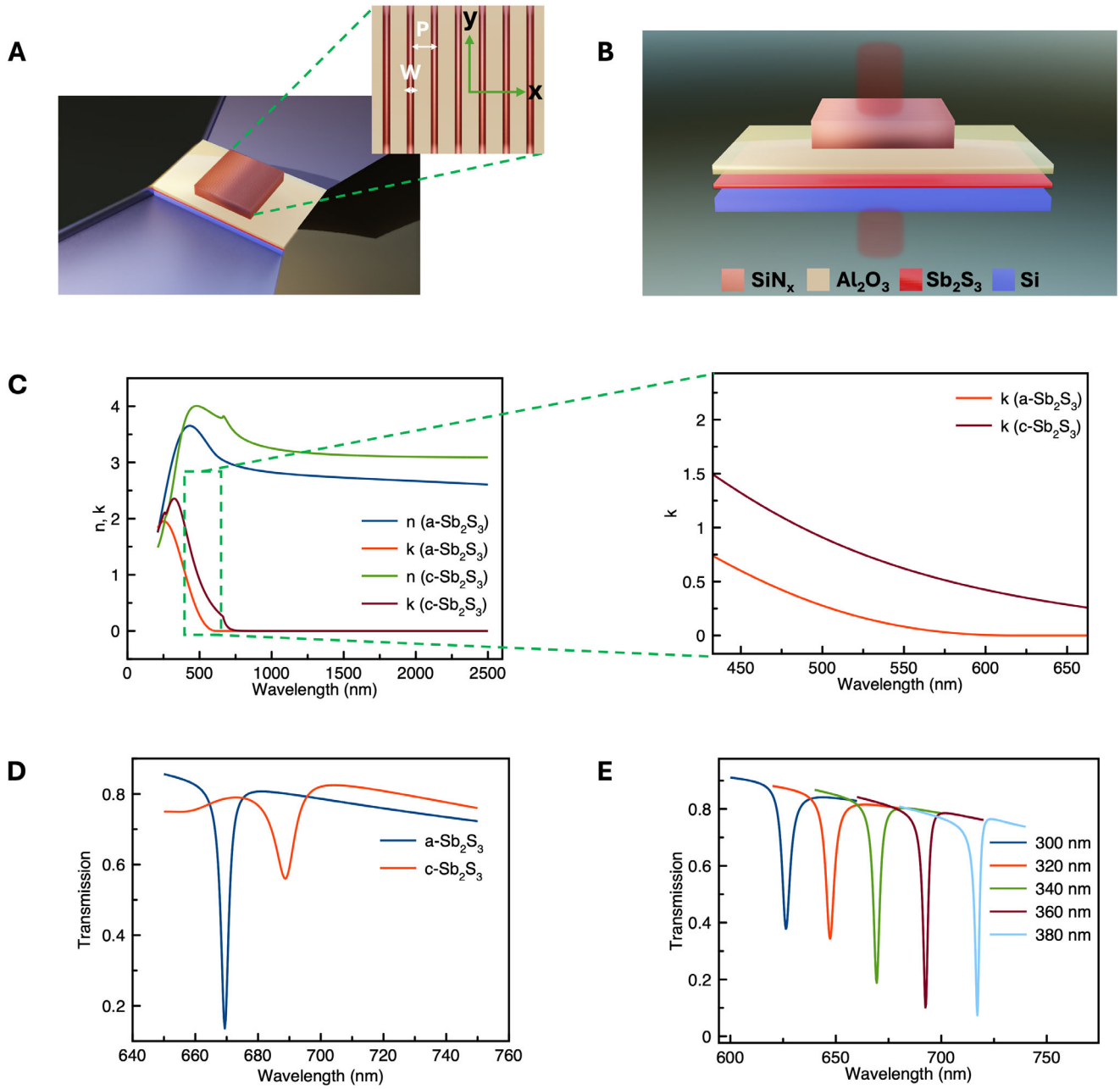

FIGURE 1 | Design of the reconfigurable metasurface. (A) Perspective view of the device with the metasurface and the electrodes. Zoomed-in is the top view of the SiN_x periodic grating with width (W) and period (P). (B) Side view of the metasurface with its 4 different layers. (C) Measured refractive index of Sb_2S_3. The zoomed-in plot on the right displays the losses of Sb_2S_3 in visible wavelengths. (D) Simulated transmission spectra when Sb_2S_3 is in its a- and c- states. (E) Transmission spectrum in simulation as we sweep the period of the SiN_x grating.

a metasurface with a Si layer thickness of 150 nm). The Q-factors for the 150, 100, 55, and 30 nm layer thicknesses are 116, 182, 230, and 817, respectively. We note that while a 30 nm Si layer gives the highest Q-factor of 817, we used a 55 nm thick Si layer to avoid an increase in resistance with decreasing Si thickness. We show in Figure S5 that a 30 nm thick Si layer can be integrated to make a metasurface guided mode resonator (GMR) [32] operating over the whole visible wavelength range from 450 to 750 nm.

Figure 2D presents the transmission spectra with varying thickness of the PCM layer. The resonance shifts to a longer wavelength with a thicker PCM. A 20 nm thickness was picked to produce a resonant wavelength well within the visible frequency range. This resonance also shows a high contrast of 72% at 670 nm wavelength, where the contrast is calculated as $(T_{max} - T_{min})/(T_{max} + T_{min})$. We emphasize that the resonance allows such a thin layer of PCM to produce a large resonance shift. A thin PCM layer is advantageous for reversible switching, as a larger volume of PCM suffers more from issues such as temperature nonuniformity and thermal reflowing. Besides, the melt and quench process demands a fast enough quench rate of $\sim 10^{-9}\ K/s$, ultimately limiting the maximum thickness of the PCM layer [13]. Figure 2E shows the spectrum of a-Sb_2S_3 with varying grating width, indicating its strong effect on both

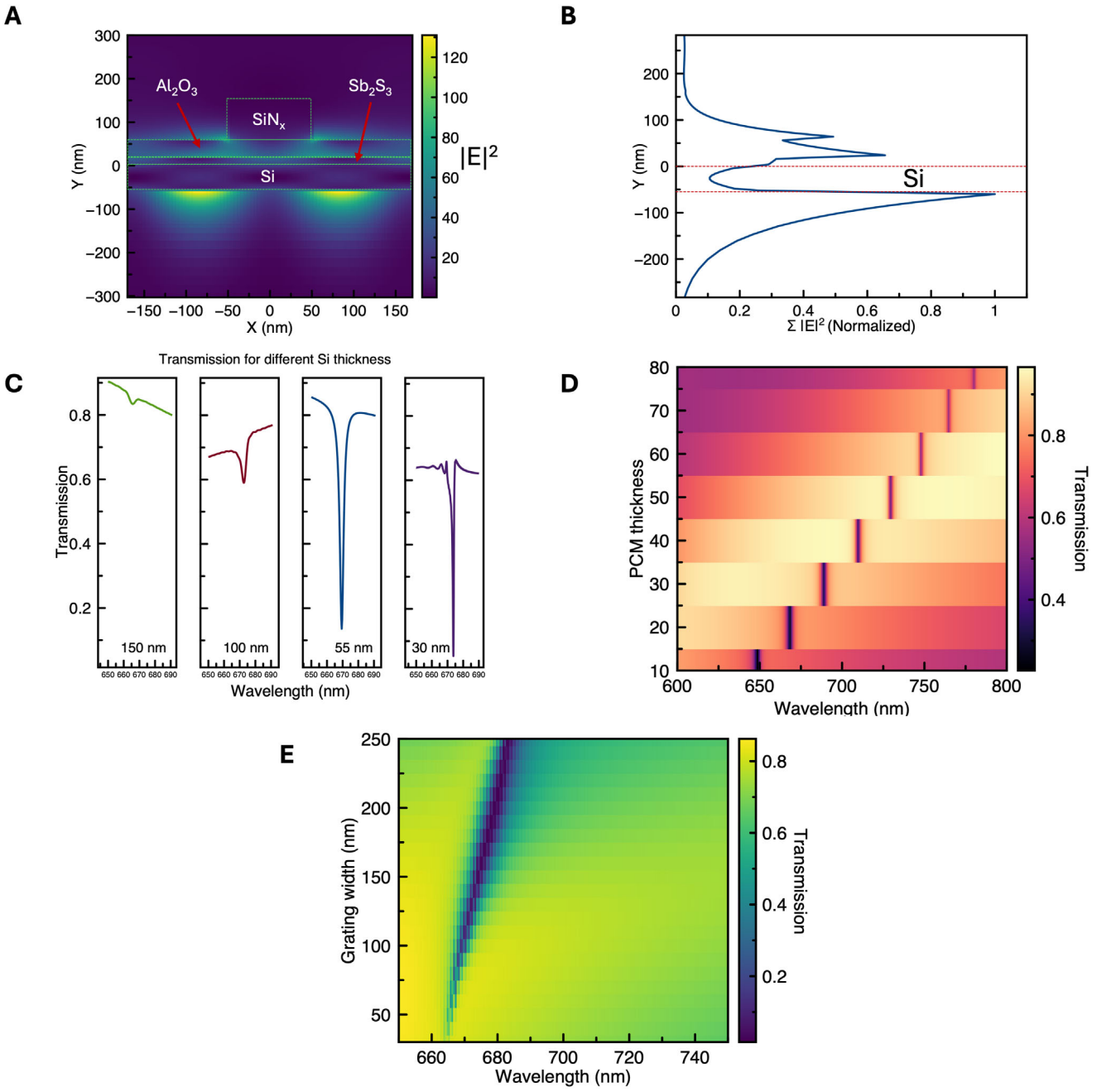

FIGURE 2 | Design optimization. (A) The $|E|^2$ inside the unit cell at resonance. (B) Sum of the E-field intensity along the thickness of the device. The red dotted lines depict the Si layer. (C) The spectra for different values of Si slab thickness. (D) The change in Transmission spectra of the device as the thickness of the PCM layer is varied. (E) Simulated Transmission spectra for different grating widths.

extinction ratio and linewidth. We design the grating width as 100 nm because it can support a resonance with a high Q-factor of 230, while remaining compatible with the critical dimension of our lithography tool. More details on the fabrication of the sample are given in the Methods section.

Several devices of different sizes were fabricated on the same chip. Figure 3A shows the micrograph of a $100 \times 100\ \mu m^2$ device before and after Rapid Thermal Annealing (RTA) at 325°C for 10 mins under an inert environment. The formation of large crystallites is evident under the microscope. The different colors of Sb_2S_3 crystallites could be attributed to the anisotropic nature of Sb_2S_3 [33]. The birefringent nature of the material does pose a challenge to achieving a deterministic index contrast. This can be mitigated by averaging out the anisotropic effect of the material by decreasing the crystal grain size or by increasing the PCMs nucleation density [21, 33]. Figure 3B presents the Scanning Electron Microscope (SEM) image of one of the devices with a period of 350 nm, showing a smooth side wall. Devices with different periods were measured in a transmission setup, see Figure S6 for a description of the setup. A 10× objective with NA 0.26 was used to illuminate the sample. A confocal pinhole was used to further reduce the angle of the incident light cone on the sample, allowing only the desired device to be illuminated

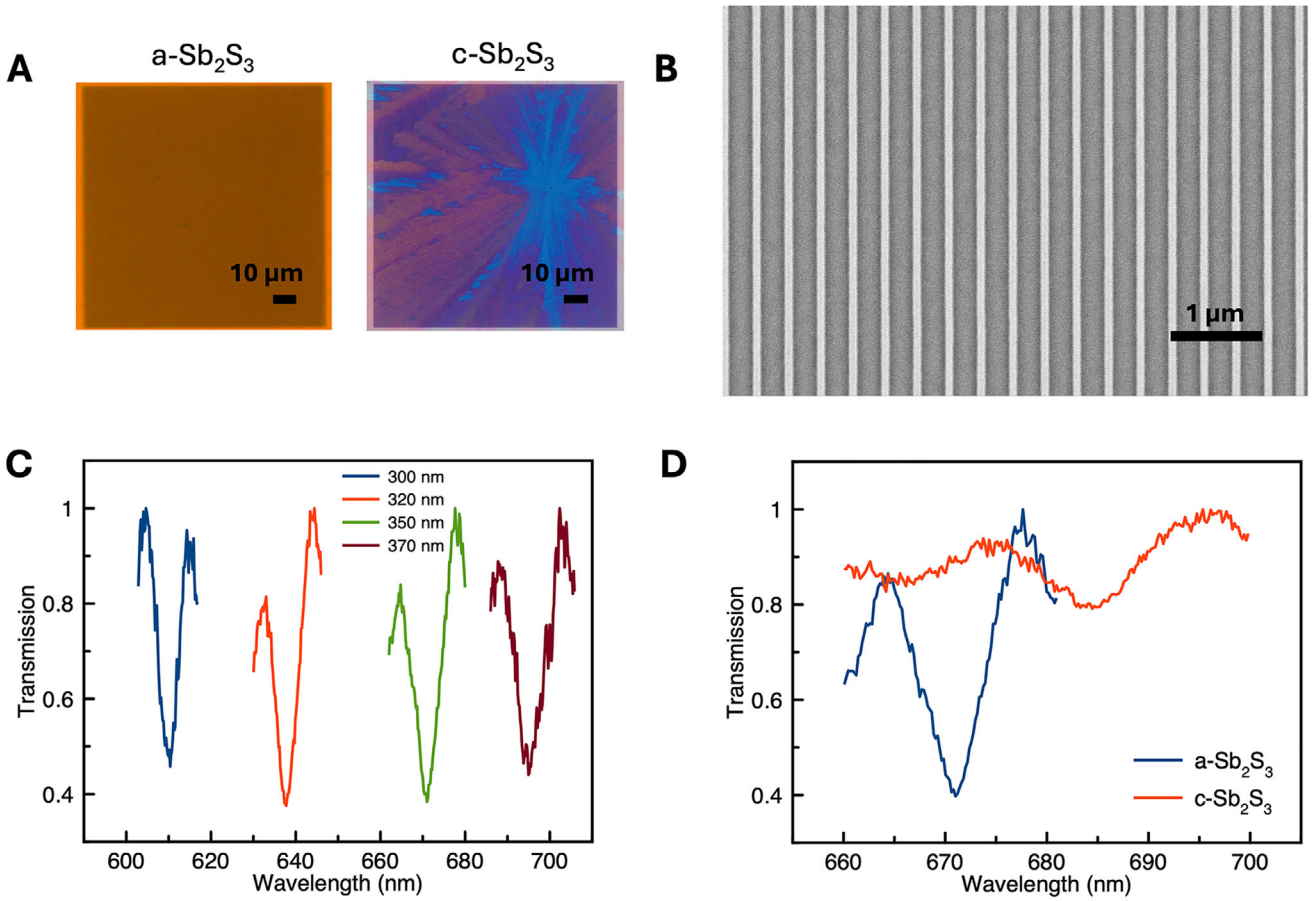

FIGURE 3 | Measurements of the fabricated device. (A) Micrographs of the 100 × 100μm^2 devices before (left) and after (right) RTA. (B) The Scanning Electron Microscope image of one of the fabricated devices. (C) The spectrum of different devices with increasing unit cell periodicity. (D) The spectrum of the device before and after RTA.

for measurement with near normal angle of incidence. The transmitted light was then collected using a 50× objective with NA 0.65 and fed to a spectrometer.

Using the setup, we first measured devices with four different periods (300, 320, 350, and 370 nm) with the PCM in a- state. As expected from simulations, an increase in the period of the unit cell results in a linear (see Figure S7) redshift of the resonant mode [32] as shown in Figure 3C. In Figure 3D, we show the spectrum of the 100 × 100 μm^2 device before and after RTA. The calculated transmission contrast at 671 nm is 38%, and the red shift in resonance is 14 nm. The experimental Q-factors calculated by fitting the spectrum using the Fano model [34] were found out to be 80 and 57 for Sb_2S_3 in a- and c- state respectively. The lower Q factors in the experiment as compared to simulation could be because of additional losses of doped Si as compared to undoped Si, and a non-ideal incident angle due to the presence of an objective.

Lastly, we perform electrical switching of the metasurface through the in situ doped silicon heaters and two metal contact pads (see Methods section for the fabrication process). Electrical signals were applied by an arbitrary function generator through two probe positioners, which are integrated with the free-space setup. A picture of the setup is shown in Figure S8. Since the power required to attain the switching temperatures scales with the area of the device [35], we attempted to switch devices with a smaller area first. Figure 4A shows a 17 × 17 μm^2 device that was switched under a microscope. We observed a reversible change in color upon applying 30 V 3.5 μs (12.6 μJ) pulse with 21 ns rise and fall times, and 15.4 V 1 μs (0.96 μJ) pulses with 21 ns rise and fall times at 500 kHz for amorphization and crystallization, respectively, as shown in Figure 4B. Video recordings of the switching under the microscope are given in Movies S1 and S2. We also show the optical micrographs of the same device under different crystallization pulse conditions in Figure S9.

Following this, we switched to a larger (20 × 20 μm^2) device with a unit cell period of 350 nm in the transmission setup shown in Figure 4C. The electrical pulses applied for inducing amorphization and crystallization were 25 V 9 μs (22.5 μJ) with a 21 ns rise and fall time and 12.5 V 100 ms (62.5 mJ) with a 21 ns rise and fall time, respectively. We reversibly switch the device for 10 cycles and plot the resonance shift in Figure 4D. The slight change in the resonance wavelength in the c-state over the cycles is attributed to multiple crystalline phases of Sb_2S_3 [15]. Additionally, recrystallization of the material after amorphization results in slightly different grain sizes and orientations, as seen in Figure 4B, on comparing the leftmost and rightmost micrograph. The resonance shift corresponding to the last cycle is 16 nm. We note that the device did not become dysfunctional after 10 cycles, but shows significant structural changes, notably the buckling

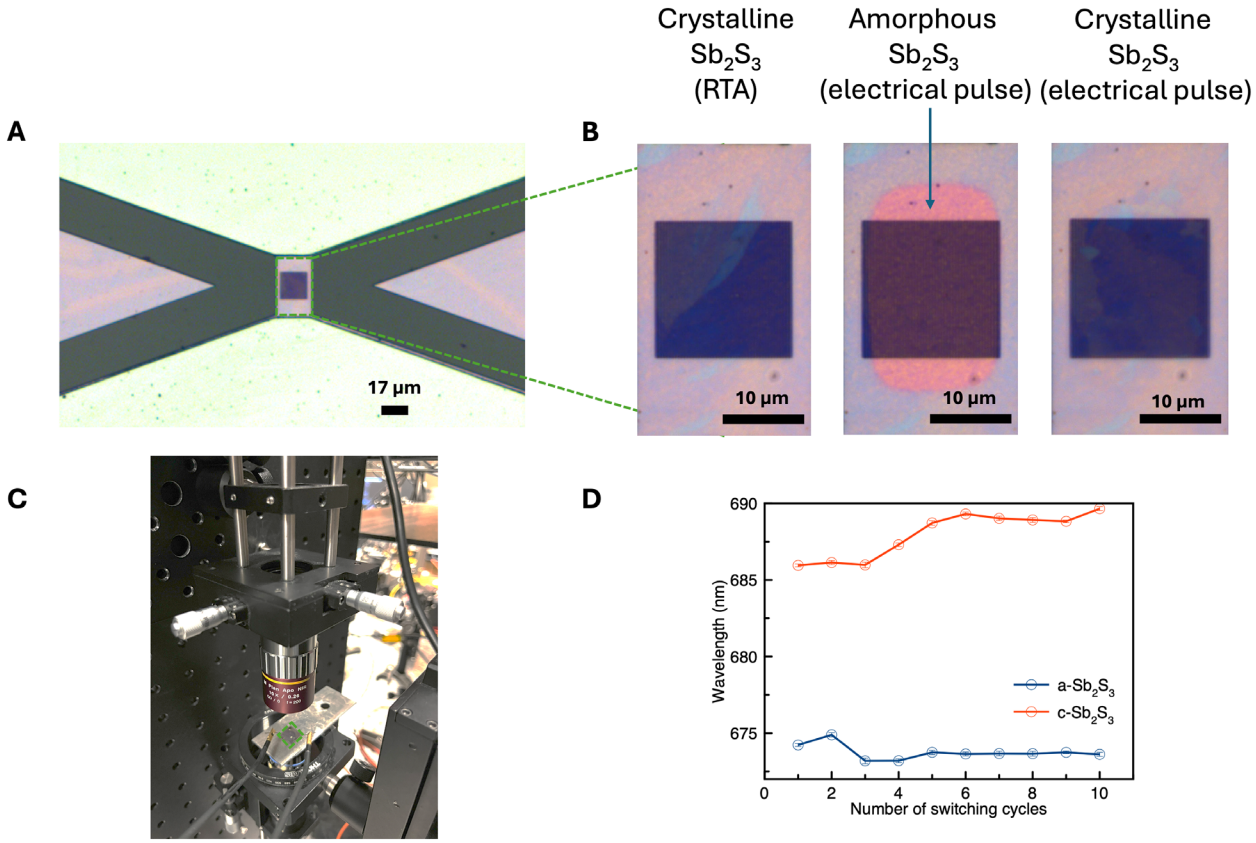

FIGURE 4 | Reversible switching using electrical pulses. (A) The micrograph of a $17 \times 17 \mu m^2$ device with contact pads for electrical switching. (B) The micrographs of the device in (A) after RTA (leftmost), after application of amorphization pulse (center), and after application of crystallization pulse (rightmost). (C) The transmission setup with probe stationers is used for the measurements. The highlighted portion is the sample. (D) The 10 cycles of switching of Sb_2S_3 and the resonance shift induced by it. Error bars depict the data fitting errors.

of the capping layer under the microscope. The micrograph of the device after 10 cycles and the transmission spectrum for 10 cycles are given in Figures S10 and S11. The structural changes are attributed to the dewetting of the PCM at the time of amorphization, when the material is in its liquid state. This issue could be resolved by restricting the movement of the material in the in-plane direction by forming isolated PCM meta-atoms, as proposed in [36], or by using a fishnet-type metasurface design, which is more suitable for growth-dominated PCMs such as Sb_2S_3 [37]. The Q-factor shows minimal variation between the first and the last recorded switching cycle 64 (63) and 71 (62) for a- (c-) states, respectively. The Q-factor for a- state is less than for a larger device reported in Figure 3D because the excited GMR is non-local and therefore requires a large number of periods to imitate ideal/ simulation results [38]. Beyond 1D resonance, we also designed and measured an ultra-thin 2D GMR metasurface, with results presented in Figure S12.

3 | Discussion

Future work includes solving the issue of structural change due to dewetting, such as by patterning the PCM into smaller patches [36] or by choosing optimal capping layers [39] with proper wetting properties. As visible in Movie S2 and as reported earlier [21], the crystallization of the material is dominated by growth rather than by nucleation. Therefore, it is desired to increase the nucleation density of Sb_2S_3, which speeds up the crystallization process and improves the material reliability. One potential solution is to use a thin ZnS layer between the substrate and the PCM, which reduces the crystal grain size significantly from 10 μm to 2–3 μm [21]. We also propose a high-throughput characterization scheme designed to assess the endurance and cyclability of tunable photonic devices at their maximum intrinsic switching speeds in Figure S13. As another future research direction, it is highly desired to extend the transparency window of PCMs to the green and blue wavelengths. PCMs like MnTe [40, 41] with an even wider band gap (2.7 eV) than Sb_2S_3 need to be investigated further for integration into photonic platforms. We also provide a comparison of our work to other non-volatile reconfigurable metasurfaces in Table S1. Lastly, rather than using a standard uniformly doped Si heater, an inverse-designed Si heater [42, 43] with a non-uniform doping profile can be utilized to ensure uniform heat delivery over a large metasurface area.

In conclusion, we demonstrated visible-frequency reconfigurable metasurfaces using a wide bandgap PCM, Sb_2S_3. An ultra-thin layer of 20 nm PCM provides a resonance shift of as large as 16 nm. The metasurface is tunable with carefully engineered, thin doped Si microheaters in the visible frequency regime, despite its inherent losses. We then validated the functionality of our design through measurements of the fabricated devices, demonstrating resonance spectra shift with different unit cell periodicity. The resonance shift of around 16 nm was verified

with RTA and followed by in situ reversible switching of the PCM through the integrated heaters, demonstrating over 10 switching cycles. Our work paves the way for applications of PCMs in the visible frequency regime and can enable the development of next-generation displays.

4 | Materials and Methods

Fabrication: The devices were fabricated on a 230 nm-doped silicon-on-sapphire wafer. Firstly, Si was doped using Phosphorus ions and annealed, resulting in a uniform doping concentration of $10^{20}cm^{-3}$ along the depth of Si. Then, the Si layer was thinned down to 55 nm using reactive ion etching (RIE) with fluorine gas (Oxford PlasmaLab 100). Then, 20 nm of Sb_2S_3 (sputtering target from PlasmaMaterials) was deposited using sputtering (Lesker Lab18) and covered with 40 nm Al_2O_3 using atomic layer deposition (Oxford PlasmaLab 80plus). At the very top, 100 nm of SiN_x was deposited using plasma-enhanced chemical vapor deposition (SPTS SPM). Finally, the top SiN_x layer was patterned using 100 kV electron-beam lithography (JEOL 6300FS) and etched using RIE with Fluorine gas (Oxford PlasmaLab 100). To put metal pads for electrical switching, the SiN_x, Sb_2S_3, and Al_2O_3 layers were removed from the area to form electrical contact between the metal and doped silicon. NR9G-3000PY photoresist was used as an etching mask and exposed using laser direct write lithography (Heidelberg DWL66+). The films were removed using RIE with Fluorine gas for SiN_x and Chlorine gas for Sb_2S_3 and Al_2O_3. Finally, Ti/Pt were deposited using sputtering (Evatec LLS EVO) and lifted off using NR9G-3000PY again, patterned using laser direct write lithography. The final device resistance was ~250 Ohms for both 17×17 and $20 \times 20\ \mu m^2$ devices.

Setup: The sample was illuminated using a broadband laser (Fianium WhiteLase Micro). The laser light was first collimated using Lens 1 and then focused onto the sample using a 10x objective (Objective 1) with a numerical aperture (NA) of 0.26. The Dichroic Mirror 1 is used to deflect the reflected light from the metasurface to a camera, along with an imaging lens (Lens 2). The transmitted light from the sample is collected using a 50× objective (Objective 2) with NA 0.65 and again split into another camera with an imaging lens (Lens 3). Finally, the laser light is fiber-coupled using Lens 4 and fed to the spectrometer (IsoPlane SCT 320 by Princeton Instruments). The electrical measurements were carried out using a pair of electrical probes on two probe positioners (Cascade Microtech DPP105-M-AI-S). The electrical pulses were generated by a pulse function arbitrary generator (Keysight 81160A) and amplified using a Cleverscope CS1070 with a 50 Ω output connected to the 250 Ω load (our device). The voltage drop on the device was calculated as $V_{device} = V_{applied} \times \frac{R_{device}}{R_{device}+R_{out}}$.

Author Contributions

A.M., R.C., and V.T. conceptualized the project. V.T. performed the simulations, fabrication, and experiment. R.A. helped with the simulations. A.T. helped with the fabrication. The setup used for measurements was built by J.F. and A.K. Models used to fit ellipsometry data of Sb_2S_3 were made by R.C., A.M., and J.J. supervised the project. V.T. wrote the manuscript with input from all the authors.

Acknowledgements

The work is supported by the DARPA-ATOM program. Part of this work was conducted at the Washington Nanofabrication Facility/Molecular Analysis Facility, a National Nanotechnology Coordinated Infrastructure (NNCI) site at the University of Washington, with partial support from the National Science Foundation via awards NNCI-1542101 and NNCI-2025489.

Funding

DARPA-ATOM, NNCI-1542101, NNCI-2025489.

Conflicts of Interest

The authors declare no conflicts of interest.

Data Availability Statement

The data that support the findings of this study are available from the corresponding author upon reasonable request.

References

1. J. E. Fröch, L. Huang, Z. Zhou, et al., "Full Color Visible Imaging with Crystalline Silicon Meta-optics," *Light: Science & Applications* 14, no. 1 (2025): 217, https://doi.org/10.1038/s41377-025-01888-w.

2. J. E. Fröch, P. Chakravarthula, J. Sun, et al., "Beating Spectral Bandwidth Limits for Large Aperture Broadband Nano-optics," *Nature Communications* 16, no. 1 (2025): 3025, https://doi.org/10.1038/s41467-025-58208-4.

3. A. Tittl, A. Leitis, M. Liu, et al., "Imaging-based Molecular Barcoding with Pixelated Dielectric Metasurfaces," *Science* 360, no. 6393 (2018): 1105–1109, https://doi.org/10.1126/science.aas9768.

4. A. Wirth-Singh, J. Xiang, M. Choi, et al., "Compressed Meta-optical Encoder for Image Classification," *Advanced Photonics Nexus* 4, no. 2 (2025): 026009, https://doi.org/10.1117/1.APN.4.2.026009.

5. H. Jiang, E. Maqbool, Y. Cai, and Z. Han, "Efficient Thermo-Optic Switching and Modulating in Nonlocal Metasurfaces," *Nano Letters* 24, no. 46 (2024): 14671–14677, https://doi.org/10.1021/acs.nanolett.4c03801.

6. E. Klopfer, S. Dagli, D. I. Barton, M. Lawrence, and J. A. Dionne, "High-Quality-Factor Silicon-on-Lithium Niobate Metasurfaces for Electro-optically Reconfigurable Wavefront Shaping," *Nano Letters* 22, no. 4 (2022): 1703–1709, https://doi.org/10.1021/acs.nanolett.1c04723.

7. P. Moitra, X. Xu, R. Maruthiyodan Veetil, et al., "Electrically Tunable Reflective Metasurfaces with Continuous and Full-Phase Modulation for High-Efficiency Wavefront Control at Visible Frequencies," *ACS Nano* 17, no. 17 (2023): 16952–16959, https://doi.org/10.1021/acsnano.3c04071.

8. Z. Fang, R. Chen, J. E. Fröch, et al., "Nonvolatile Phase-Only Transmissive Spatial Light Modulator with Electrical Addressability of Individual Pixels," *ACS Nano* 18, no. 17 (2024): 11245–11256, https://doi.org/10.1021/acsnano.4c00340.

9. V. Tara, R. Chen, J. E. Fröch, et al., "Non-Volatile Reconfigurable Transmissive Notch Filter Using Wide Bandgap Phase Change Material Antimony Sulfide," *IEEE Journal of Selected Topics in Quantum Electronics* (IEEE, 2024), 1–8, https://doi.org/10.1109/JSTQE.2024.3430214.

10. R. Audhkhasi, V. Tara, M. Klein, et al., "Electrically Reconfigurable Nonvolatile Flatband Absorbers in the Mid-Infrared with Wide Spectral Tuning Range," *Nano Letters* 25, no. 36 (2025): 13533–13538, https://doi.org/10.1021/acs.nanolett.5c03023.

11. J. Li, C.-H. Wen, S. Gauza, R. Lu, and S.-T. Wu, "Refractive Indices of Liquid Crystals for Display Applications," *Journal of Display Technology* 1, no. 1 (2005): 51–61, https://doi.org/10.1109/JDT.2005.853357.

12. H. Sun, C. Lian, F. Vásquez-Aza, et al., "Microheater Hotspot Engineering for Spatially Resolved and Repeatable Multi-level Switching in Foundry-processed Phase Change Silicon Photonics," *Nature*

Communications 16, no. 1 (2025): 4291, https://doi.org/10.1038/s41467-025-59399-6.

13. Z. Fang, R. Chen, V. Tara, and A. Majumdar, "Non-volatile Phase-change Materials for Programmable Photonics," *Science Bulletin* 68, no. 8 (2023): 783–786, https://doi.org/10.1016/j.scib.2023.03.034.

14. O. Hemmatyar, S. Abdollahramezani, I. Zeimpekis, et al., "Enhanced Meta-Displays Using Advanced Phase-Change Materials," *arXiv* (2021): arXiv:210712159, https://doi.org/10.48550/arXiv.2107.12159.

15. "Rewritable Color Nanoprints in Antimony Trisulfide Films | Science Advances," accessed August 11, 2025, https://www.science.org/doi/full/10.1126/sciadv.abb7171.

16. L. Lu, Z. Dong, F. Tijiptoharsono, et al., "Reversible Tuning of Mie Resonances in the Visible Spectrum," *ACS Nano* 15, no. 12 (2021): 19722–19732, https://doi.org/10.1021/acsnano.1c07114.

17. W. Dong, H. Liu, J. K. Behera, et al., "Wide Bandgap Phase Change Material Tuned Visible Photonics," *Advanced Functional Materials* 29, no. 6 (2019): 1806181, https://doi.org/10.1002/adfm.201806181.

18. "Aperiodic Bragg Reflectors for Tunable High-Purity Structural Color Based on Phase Change Material | Nano Letters," accessed November 27, 2025, https://pubs.acs.org/doi/full/10.1021/acs.nanolett.4c00052.

19. Z. Han, C. Li, T. Liu, et al., "Electrically Reconfigurable Plasmonic Metasurfaces Based on Phase-Change Materials Sb2S3," *Nano Letters* 25, no. 18 (2025): 7435–7441, https://doi.org/10.1021/acs.nanolett.5c00929.

20. P. Moitra, Y. Wang, X. Liang, et al., "Programmable Wavefront Control in the Visible Spectrum Using Low-Loss Chalcogenide Phase-Change Metasurfaces," *Advanced Materials* 35, no. 34 (2023): 2205367, https://doi.org/10.1002/adma.202205367.

21. M. Wu, M. K. S. Barr, V. M. Koch, et al., "Correlative and in Situ Microscopy Investigation of Phase Transformation, Crystal Growth, and Degradation of Antimony Sulfide Thin Films," *ACS Nano* 19, no. 27 (2025): 25017–25027, https://doi.org/10.1021/acsnano.5c04342.

22. J. Zhang and Y. Kivshar, "Quantum Metaphotonics: Recent Advances and Perspective," *APL Quantum* 1, no. 2 (2024): 020902, https://doi.org/10.1063/5.0201107.

23. A. S. Solntsev, G. S. Agarwal, and Y. S. Kivshar, "Metasurfaces for Quantum Photonics," *Nature Photonics* 15, no. 5 (2021): 327–336, https://doi.org/10.1038/s41566-021-00793-z.

24. W. Wan, J. Gao, and X. Yang, "Metasurface Holograms for Holographic Imaging," *Advanced Optical Materials* 5, no. 21 (2017): 1700541, https://doi.org/10.1002/adom.201700541.

25. Q. Jiang, G. Jin, and L. Cao, "When Metasurface Meets Hologram: Principle and Advances," *Advances in Optics and Photonics* 11, no. 3 (2019): 518–576, https://doi.org/10.1364/AOP.11.000518.

26. T. Y. Teo, N. Li, L. Y. M. Tobing, et al., "Capping Layer Effects on Sb_2S_3-Based Reconfigurable Photonic Devices," *ACS Photonics* 10, no. 9 (2023): 3203–3214, https://doi.org/10.1021/acsphotonics.3c00600.

27. "Non-Volatile Reconfigurable Integrated Photonics Enabled by Broadband Low-Loss Phase Change Material—Fang –2021 – Advanced Optical Materials—Wiley Online Library," accessed July 22, 2025, https://advanced.onlinelibrary.wiley.com/doi/full/10.1002/adom.202002049.

28. Z. Fang, R. Chen, J. Zheng, et al., "Ultra-low-energy Programmable Non-volatile Silicon Photonics Based on Phase-change Materials with Graphene Heaters," *Nature Nanotechnology* 17, no. 8 (2022), https://doi.org/10.1038/s41565-022-01153-w.

29. R. Colom, E. Mikheeva, K. Achouri, et al., "Crossing of the Branch Cut: the Topological Origin of a Universal 2π-Phase Retardation in Non-Hermitian Metasurfaces," *Laser & Photonics Reviews* 17, no. 6 (2023): 2200976, https://doi.org/10.1002/lpor.202200976.

30. C. L. Panuski, I. Christen, M. Minkov, et al., "A Full Degree-of-freedom Spatiotemporal Light Modulator," *Nature Photonics* 16, no. 12 (2022): 834–842, https://doi.org/10.1038/s41566-022-01086-9.

31. M. Z. Alam, X. Sun, M. Mojahedi, and J. S. Aitchison, "Augmented Low Index Waveguide for Confining Light in Low Index media," *Laser & Photonics Reviews* 11, no. 3 (2017): 1500224, https://doi.org/10.1002/lpor.201500224.

32. S. S. Wang and R. Magnusson, "Theory and Applications of Guided-mode Resonance Filters," *Applied Optics* 32, no. 14 (1993): 2606–2613, https://doi.org/10.1364/AO.32.002606.

33. F. Hoff, J. Pries, J. Köttgen, P. Lucas, and M. Wuttig, "Controlling the Crystallization Kinetics of Low Loss Phase Change Material Sb_2S_3," *Advanced Physics Research* 4, no. 9 (2025): 2500005, https://doi.org/10.1002/apxr.202500005.

34. S. Li, B. Ma, Q. Li, and M. V. Rybin, "Antenna-Based Approach to Fine Control of Supercavity Mode Quality Factor in Metasurfaces," *Nano Letters* 23, no. 14 (2023): 6399–6405, https://doi.org/10.1021/acs.nanolett.3c01141.

35. K. Aryana, C. C. Popescu, H. Sun, et al., "Thermal Transport in Chalcogenide-Based Phase Change Materials: a Journey from Fundamental Physics to Device Engineering," *Advanced Materials* 37, no. 11 (2025): 2414031, https://doi.org/10.1002/adma.202414031.

36. "Understanding and Circumventing Failure Mechanisms in Chalcogenide Optical Phase Change Material $Ge_2Sb_2Se_4Te$—Popescu –2025 – Advanced Optical Materials—Wiley Online Library," accessed July 21, 2025, https://advanced.onlinelibrary.wiley.com/doi/full/10.1002/adom.202402751.

37. C. C. Popescu, K. Aryana, P. Garud, et al., "Electrically Reconfigurable Phase-Change Transmissive Metasurface," *Advanced Materials* 36, no. 36 (2024): 2400627, https://doi.org/10.1002/adma.202400627.

38. C. U. Hail, M. Foley, R. Sokhoyan, L. Michaeli, and H. A. Atwater, "High Quality Factor Metasurfaces for Two-dimensional Wavefront Manipulation," *Nature Communications* 14, no. 1 (2023): 8476, https://doi.org/10.1038/s41467-023-44164-4.

39. L. Martin-Monier, C. C. Popescu, L. Ranno, et al., "Endurance of Chalcogenide Optical Phase Change Materials: A Review," *Optical Materials Express* 12, no. 6 (2022): 2145–2167, https://doi.org/10.1364/OME.456428.

40. T. Yazaki, M. Kuwahara, H. Kawashima, and H. Tsuda, "Proposal of a Phase-Change Optical Switch Using a Low-loss MnTe Thin Film," in *2024 IEEE Photonics Conference (IPC)* (IEEE, 2024), 1–2, https://doi.org/10.1109/IPC60965.2024.10799707.

41. S. Mori, S. Hatayama, Y. Shuang, D. Ando, and Y. Sutou, "Reversible Displacive Transformation in MnTe Polymorphic Semiconductor," *Nature Communications* 11, no. 1 (2020): 85, https://doi.org/10.1038/s41467-019-13747-5.

42. K. P. Dao and J. Hu, "Thermal Inverse Design for Resistive Microheaters," *Journal of Applied Physics* 136, no. 22 (2024): 225101, https://doi.org/10.1063/5.0235526.

43. V. Tara, K. P. Dao, J. Wei, J. Hu, and A. Majumdar, "Electrically Reconfigurable Non-Volatile Metasurface in the Visible Spectrum with an Inverse Designed Heater," *Frontiers in Optics + Laser Science 2025 (FiO, LS) (2025), paper JTu7A.2* (Optica Publishing Group, 2025), https://opg.optica.org/abstract.cfm?uri=FiO-2025-JTu7A.2.

Supporting Information

Additional supporting information can be found online in the Supporting Information section.

Supporting File 1: adom71094-sup-0001-SuppMat.docx.

Supporting File 2: adom71094-sup-0002-MovieS1.mp4.

Supporting File 3: adom71094-sup-0003-MovieS2.mp4.